

# Numerical optimization of the fin shape experiments of a heat conjugate problem surface air/oil heat exchanger (SACOC)

Miguel Chávez-Modena<sup>a,b,\*</sup>, Leo Miguel González<sup>a,b</sup>, Eusebio Valero<sup>a,b</sup>

<sup>a</sup> ETSIAE-UPM - School of Aeronautics, Universidad Politécnica de Madrid, Plaza Cardenal Cisneros 3, Madrid E-28040, Spain

<sup>b</sup> Center for Computational Simulation, Universidad Politécnica de Madrid, Campus de Montegancedo, Boadilla del Monte, Madrid, 28660, Spain

## ARTICLE INFO

### Article history:

Received 5 April 2021

Revised 10 June 2021

Accepted 10 September 2021

### Keywords:

SACOC heat exchanger

Aircraft engines

Optimization

Adjoint method

Finite volumes

Conjugate heat problem

## ABSTRACT

Efficient aircraft engine designs imply the presence of a surface air/oil heat exchanger placed at the bypass flow separation of the engine. The heat exchanger consists of several parallel longitudinal fins that increase the contact area to obtain a higher heat dissipation rate. The design of these fins is an important task as the pressure drop generated by the presence of the heat exchanger is the largest drawback to be minimized in the final setup. Consequently, an efficient design of the fins that optimizes the global performance of the heat exchanger is highly demanded. The result of this optimization process should minimize the pressure drop caused by the exchanger without decreasing the heat transfer. The optimization methodology proposed in this work is split in two independent parts: in the first one, the fin shape is optimized using the adjoint method and the derived sensitivity function that controls the position of the fin shape design. In parallel, the range of fin thickness and distance between fins was investigated to have an optimized fin distribution for a given SACOC width. Once the geometry was optimized, the coupled conjugate heat problem is numerically solved using realistic conditions showing good accuracy in the two presented validations. The result for the optimized geometry presents a substantial pressure drop reduction with little heat transfer variation, addressing the objectives that motivated the present study.

© 2021 Elsevier Ltd. All rights reserved.

## 1. Introduction

Advanced oil cooling strategies for more efficient engine architectures are one of the technological challenges that demand more intense research. New engine designs based on inlet air stream and the fuel circuit are approaching their limits as typical cold sources [1]. Complex coupled problems are found in this kind of mechanical systems, where the thermal part must be treated adequately. It should be taken into account that the heat removal by the aircraft structure will be limited using composite materials with lower operational temperature and thermal conductivity properties. Furthermore, the limitation on the maximum fuel temperature decreases the viability of the fuel tank as a cold source [2].

Therefore, a novel engine cooling strategy seems to be a new industrial demand [3]. In this context, the evaluation of the thermal performance of an Air Cooled Oil Cooler (ACOC) heat exchanger assembled on the inner wall of the secondary duct of a

turbofan, could be an interesting quantitative study. The goal of such design is to use the available surface as a heat exchanger between the air and the oil. To increase the thermal performance, the wet area is increased by adding longitudinal fins, reaching the required heat dissipation rate. Such a design implies a strong compromise between the aerodynamic penalties, quantified by the drag increase or pressure drop, and the improvement in the thermal performance of the heat exchanger. The developed research presents an optimization study of a heat exchanger in realistic flow conditions within the bypass of an engine.

This surface air/oil heat exchanger (SACOC) can be located on the lip separating the engine bypass flow from the core flow, between the fan and the downstream outlet guide vane. The SACOC is used to evacuate, in the bypass air stream, a large quantity of heat contained in the oil (contributing therefore to the thrust of the engine) with minimal perturbation and therefore a minimal impact on Specific Fuel Consumption (SFC). The coolant source is the bypass mass flow delivered by the fan. Indeed, the performance of the SACOC is measured in terms of maximum heat release capacity with minimal perturbation of the flow, in terms of pressure losses and acoustic emission.

\* Corresponding author at: ETSIAE-UPM - School of Aeronautics, Universidad Politécnica de Madrid, Plaza Cardenal Cisneros 3, Madrid E-28040, Spain.

E-mail address: [m.chavez@upm.es](mailto:m.chavez@upm.es) (M. Chávez-Modena).

## Nomenclature

$X, Y, Z$	cartesian axis
$x, y, z$	spatial coordinates
$u_i$	$i$ th component of the velocity field
$u'_i$	$i$ th component of the turbulent deviation of the fluid velocity
$p$	pressure field
$u_{exp}$	experimental inflow profile
$T$	temperature field
$\theta$	conjugate boundary temperature
$T_\infty$	inflow temperature
$\mathbf{n}$	wall normal direction
$U_\infty$	maximum inflow velocity
$\rho_\infty$	inflow density
$p_s$	outflow static pressure
$L, H, W$	domain dimensions
$LFIN, HFIN, WF, SFIN, LU, LD$	SACOC geometrical dimensions
$a, b, LB, HB, WB$	base geometrical dimensions
$\rho$	fluid density
$\dot{Q}$	heat transfer per time unit
$\dot{m}$	mass flow
$Re$	Reynolds number
$A_{xy}$	lateral fin area
$N$	number of control points
$Pr$	Prandtl number
$Nu$	Nusselt number
$M$	Mach number
$\mu$	fluid viscosity
$\nu$	fluid kinematic viscosity
$d_h$	hydraulic diameter
$w$	average air velocity
$V$	volumetric flow rate
$k$	thermal conductivity
$R_{th}$	thermal resistance
$\delta$	boundary layer thickness
$\Delta p$	pressure drop
$C_p$	specific heat capacity
$T_c$	temperature at the bottom of the fins
$h$	local heat transfer coefficient
$h_g$	global heat transfer coefficient
$A_f$	total fin area
$H_c$	characteristic mesh size close to the fin surface
$H_{fin}$	characteristic fin mesh size

Surface Air Cooled Oil Coolers are normally composed of parallel fins integrated in the inner wall of the secondary duct of a turbofan. The geometrical characteristics and location of the fins within the engine are designed to minimize aerodynamic effects (drag and noise increments) while maximizing thermal exchange. This heat exchanger configuration introduces less aerodynamic perturbations than current plate/tube heat exchanger modules. These losses were estimated at approximately 1% for the full annular section of a turbofan with a bypass ratio equal to 6 [4]. The analysis of the interaction between the three-dimensional high velocity bypass flow and the heat exchangers is essential to evaluate and optimize the aero-thermodynamic performance, and to provide data for engine modelling.

We should remark that despite much literature can be found regarding the heat exchangers in, for example, the electronic in-

dustry [5,6], here we are particularly interested in the flow and temperature conditions present in aircraft engine applications. This SACOC heat exchanger concept was designed to reproduce the bypass flow of a high-bypass ratio turbofan at the most critical operational point for the oil thermal system, i.e., cruise velocity and take-off atmospheric conditions. The use of heat exchangers interacting with the engine bypass flow has been proposed in many patents [7–10], also the open literature provides numerous references [11–13].

The geometry involved in the heat exchange is one of the most critical variables of the system performance. Starting from the simplest case where forced convective heat transfer in a boundary layer flow was studied over a flat plate by Pelerman [14] and Vynnycky et al. [15], other fin geometries such as plates, strips, and pins can be used as heat sinks giving different performance. The performance of plate fin heat sinks has been studied extensively by Sparrow and co-workers [16–18], Lau and Mahajan [19], Wirtz and co-workers [20,21] by experimental tests, numerically and analytically by Kadle and Sparrow [22], Sata et al. [23] and Jonsson and Moshfegh [24,25] and both experimentally and numerically by Iwasaki et al. [26].

The heat transfer enhancement by introducing strip fins and its comparison between plate and staggered strip fin heat sinks has been studied by Sparrow [27,28] for laminar flow cases, and by other authors [29–31].

An exhaustive review of the heat-exchange technology applied to cooling-air cooler applications was performed by Min et al. [32], and particularized for cooling oil systems in Kim et al. [33]. The surface air-oil heat exchanger (SACOC) is located inside the engine fan casing, and dissipates the heat from the oil into the air stream in the bypass duct (BPD), as shown in Fig. 1. The main difficulty of SACOC design is the existence of the bypass stream, which affects the pressure drop inside the bypass duct. There have been a number of studies aimed at enhancing aero-thermal performance by varying the fin shape of the heat exchanger. It was found that a modified fin surface may have a high heat transfer coefficient, but that its pressure drop is sometimes excessive for wide applications.

Several studies using computational fluid dynamics (CFD) have been extensively applied to the study and comparison of different SACOC designs. Kim et al. [34] compared numerically the performance of a plate and pin-fin shaped geometry as the surface of an air-oil heat exchanger. Basic heat transfer and pressure drop characteristics were examined using a simplified channel model. Using a parametric study, the optimal fin pitches of the pin-fin geometries in stream- and spanwise directions were determined. Finally, the high-speed bypass effect of the surface air-oil heat exchanger was calculated using the geometry of a real engine. He also examined [33] the sensitivity of finned coolers to perturbations on their location and orientation using RANS simulations. Another numerical comparison between the aerodynamic disturbances caused by heated fins, where two different designs, continuous and interrupted fins were tested in Sousa et al. [4].

Regarding the experimental approach to the problem in realistic conditions, a particular air/oil heat exchanger design, see Fig. 1, composed by fins aligned with the flow direction and integrated in the surface of the core/bypass flow splitter, downstream of the flow bifurcation was studied in Villafañe and Paniagua [35]. We should also mention the experimental contribution based on the sensitivity of the complex transonic and three-dimensional turbofan bypass-flow to arrays of fins embedded on the splitter is performed by Villafañe and Paniagua [35]. They assess the flow modifications introduced by two different fin heat exchanger designs, with *continuous* and *interrupted* fins. This work demonstrates the importance of aerodynamically optimized designs to minimize detrimental effects on propulsive efficiency.

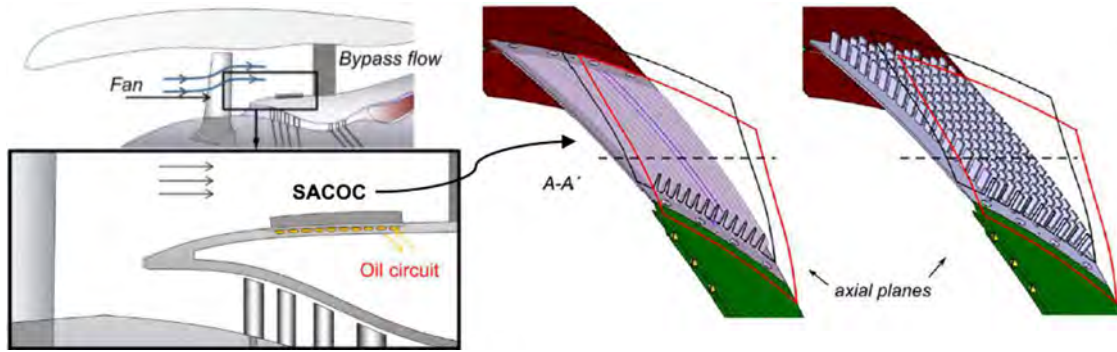


Fig. 1. EPNdB configuration studied by UPV, VKI and Purdue University [4,35].

The goal of this work is clear, given the typical SACOC design and flow conditions, we will develop a strategy to optimize the design of the fin geometry and setup to minimize the pressure drop due to the exchanger while keeping the heat transfer. Previous works based on shape optimization problems can be found in Morimoto et al. [36], Gkaragkounis et al. [37], Subramaniam et al. [38] but most of these studies are not referred to the conjugate heat transfer problem and just optimize the shape of a body in terms of drag, or are far from the flow conditions expressed here.

This work is organised as follows: First, the numerical methodology is presented in Section 2. Then, a validation of the multi-physics methodology for a 2D flat plate and a 3D finned geometry is performed and compared with the experimental results in Section 3. Finally, in Section 4 the optimization methodology is explained and applied to a realistic SACOC geometry, the problem is solved for the optimized geometry and compared to the original one.

## 2. Numerical methodology.

### 2.1. Description of the problem.

In this section, we are going to simplify the intrinsic complexity that is found in the technological problem described in Section 1. The first step is to use a simplified geometrical model to examine the aero-thermal performance of a finned surface in a reduced part of the global geometry. In this simplified geometry, the slight curvature of the model normally present in industrial designs will be neglected in the computational domain. The modeled geometry is formed by fins lying on a flat base which is heated through its lower surface. The fin and base are both made up of aluminium. The coordinate system is such that the X axis follows the stream-wise direction, the Y axis is in the vertical direction and Z axis is orthogonal to the XY plane. Due to the symmetry of the problem, only half of the complete geometry (only 8 of the 16 fins) will be considered for the computations, see Fig. 2. The geometrical parameters shown in Fig. 2 are defined in Table 2.

The configuration shown in Fig. 2 is used for the analysis of the fin geometrical parameters of Sections 4.3.1 and 4.3.2. However, when tasks such as the shape fin optimization performed in Section 4.3.3, a periodic single fin geometry is used, see Fig. 3, which implies fewer cells and consequently there is less computational demand.

### 2.2. Governing equations and boundary conditions

The conjugate heat transfer problem couples a turbulent compressible flow to the heat transfer coming from a finned surface. The problem domain can be decomposed in two parts: the fluid part ruled by the compressible Reynolds-averaged Navier–Stokes

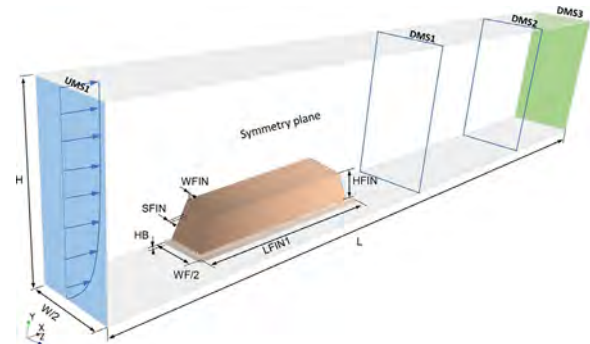


Fig. 2. Computational scheme of one half of 3D symmetric finned geometry tested.

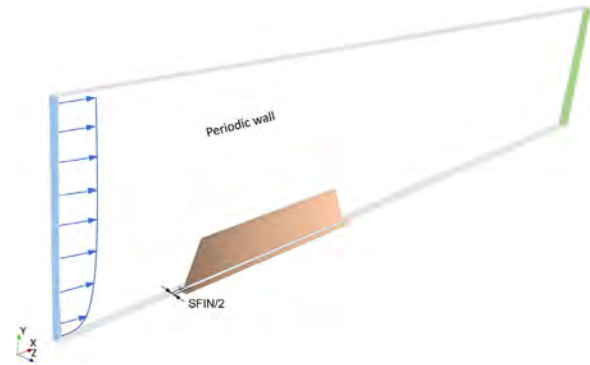


Fig. 3. Computational scheme of the periodic 3D geometry tested.

(RANS) equations, and the solid part where a heat transfer problem is solved. Both problems are coupled by the appropriate compatibility conditions through the cooling fin surface, where no-slip velocity, temperature, and heat flux continuity are applied. When possible, the distances will be non-dimensionalized with the length of the fins in the flow direction LFIN, velocity with the maximum inflow value  $U_\infty$ , density with the inflow value  $\rho_\infty$  pressure with the outflow static pressure  $p_s$ , and temperatures as the Conjugate Boundary Temperature,  $\theta = \frac{T - T_\infty}{\Delta T}$ , where  $T_c$  is the temperature at the bottom of the base and  $\Delta T = T_c - T_\infty$  is the temperature difference between the heated wall base and the inflow. Below, the subindexes  $f$  and  $s$  are used to determine the fluid and solid temperature regions, respectively.

Considering the air as an ideal gas, the continuity, momentum, and energy non-dimensional equations for the steady, compressible, and turbulent flow are:

$$\frac{\partial \rho u_i}{\partial x_i} = 0, \tag{1}$$

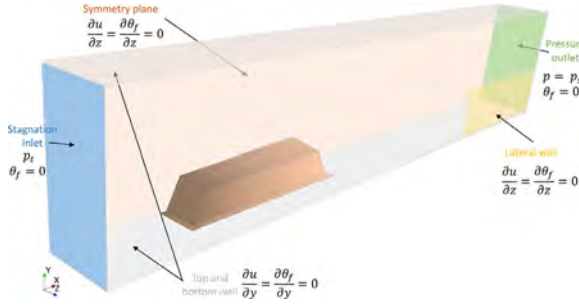


Fig. 4. Boundary conditions imposed at the different surfaces of half fluid domain (symmetric hypothesis).

$$\frac{\partial \rho u_i u_j}{\partial x_j} = \frac{\partial p}{\partial x_i} + \frac{\partial}{\partial x_j} \left[ \frac{1}{Re} \left( \frac{\partial u_i}{\partial x_j} + \frac{\partial u_j}{\partial x_i} \right) - \rho \overline{u'_i u'_j} \right], \quad (2)$$

$$\frac{\partial \rho u_i \theta_f}{\partial x_i} = - \frac{\partial}{\partial x_i} \left( - \frac{1}{Re Pr} \frac{\partial \theta_f}{\partial x_i} + \rho \overline{u'_i \theta'_f} \right), \quad (3)$$

where  $\rho$  is the fluid density,  $u_i$  is the fluid velocity in the  $i$  direction,  $p$  is the fluid pressure,  $u'_i$  is the turbulent deviation of the fluid velocity,  $\theta_f$  is the fluid temperature.

The SST  $k-\omega$  turbulence model is implemented to compute the eddy viscosity [39]. The equation of state for perfect gases is also added to the system (1)–(3). The dominant non-dimensional numbers are: the Reynolds number defined as  $Re = \rho_\infty U_\infty L_{FIN} / \mu$ , the Prandtl number  $Pr = C_p \mu / k_f$  and the non-dimensional conductivity  $k = k_s / k_f$ . Where  $\mu$  the fluid viscosity,  $k_f = k_{air}$  and  $k_s = k_{Al}$  the fluid (air) and solid (aluminium) conductivities respectively and  $C_p$  specific heat. Eqs. (1)–(3) are complemented with the boundary conditions shown in Fig. 4.

As the problem presents a symmetry plane  $z = 0$ , a symmetry boundary is included in the simulation, see Fig. 2.

For the inflow boundary conditions, a non-dimensional total pressure profile  $p_t(y)$ , provided by the aircraft engine company SAFRAN and considered representative of this flow configuration, a constant inflow temperature  $\theta_f = 0$ , and the turbulence intensity and viscosity ratio values are imposed.

For the outflow, a non-dimensional static pressure,  $p_s = 1$ , outlet boundary condition is used and the temperature is fixed to the inlet value,  $\theta_f = 0$ .

Adiabatic no-slip boundary conditions are used for the lateral right and top walls of the tunnel.

For the bottom wall, several zones are considered: the fins, where no slip boundary conditions are used for the velocity and heat transfer is allowed, and the region with no fins, where adiabatic and no-slip boundary conditions are assumed for temperature and velocity respectively.

The non-dimensional equation that models the heat conduction effects of the conjugate heat transfer problem in the solid region inside the fins is:

$$\nabla^2 \theta_s = 0, \quad (4)$$

where  $\theta_s$  is the solid temperature. The boundary conditions  $\frac{\partial \theta_s}{\partial n} = 0$  and  $\theta_s = 1$  are used for the fin surface and the fins horizontal base, respectively.

Additionally, the coupling between both the compressible fluid problem and the heat transfer problem is given by the CHT boundary conditions  $\theta_s = \theta_f$  and  $\frac{\partial \theta_s}{\partial n} = k \frac{\partial \theta_f}{\partial n}$  on the body/fluid interface providing the continuity of thermal fields and heat flux between the body and flow at the interface.

Similarly to the fluid case, a symmetry plane is used for the thermal problem, being the rest of the boundaries adiabatic, with

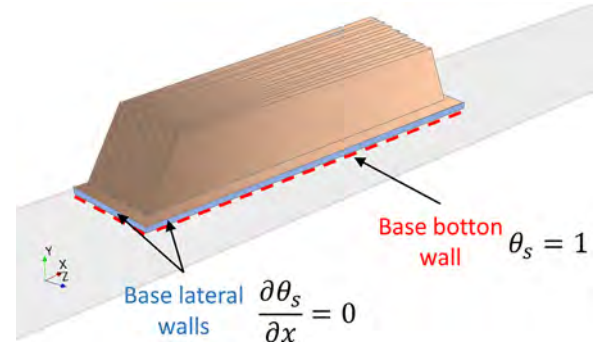


Fig. 5. Boundary conditions imposed at the different surfaces of the solid domain.

the only exception of the bottom wall which is isothermal with temperature  $\theta_s = 1$ , see Fig. 5.

In summary, the problem depends on the geometry, the inflow profile, and the parameters  $Re$ ,  $Pr$  and  $k$ .

To solve correctly the velocity boundary layer, we will ensure that  $y^+ < 1$ . As the fluid is a gas, the  $Pr \approx 1$ , the velocity and the thermal boundary layers thickness will be both equivalent  $\delta_v \approx \delta_T$ .

### 2.3. Computational tool

As compressible and turbulent effects are taken into account, the energy equation is coupled with the momentum equation and the speed of sound is not fixed. A finite volume code is used to discretize both the fluid mechanics and the heat transfer coupled problem.

The coupled system of Eqs. (1)–(3) and (4) are solved using an implicit second-order discretization method to compute the Navier–Stokes equations and to calculate the density, temperature, pressure and velocity fields at the steady state. Despite the equations are written in non-dimensional form to list the number of non-dimensional parameters that influence the problem, the internal computation of the code uses the dimensional version of the equations, and consequently when non-dimensional results such as the reduced temperature are presented they require to be postprocessed. For these steady simulations, an iterative process is used to ensure the steady state condition to be satisfied with low residuals. To accelerate the solver convergence, a coupled algebraic multigrid method [40] based on V fixed cycles is used.

For the conjugate heat transfer analysis, the energy equation is solved throughout the fluid and solid domains with an implicit thermal coupling at the fluid/solid interface. The coupling between Eqs. (1)–(3) and (4) is performed at each iteration on the body/fluid interface, forcing the continuity of the temperature field and energy conservation between the solid and the flow at the interface. In the absence of source terms at this interface, energy conservation implies heat flux continuity. These compatibility conditions are additional equations that must be satisfied in combination with the fluid and thermal subsystems to solve the coupled problem.

### 2.4. SACOC optimization

At this point, we should explain what are the optimization criteria that are followed for this kind of problem. According to the industrial criteria agreed with outstanding companies such as SAFRAN, the minimization of the pressure drop, see Eq. (5), is the main objective of the optimization process.

$$\Delta p = \frac{\int |\dot{m}| p_t}{\int |\dot{m}|} \Big|_{inlet} - \frac{\int |\dot{m}| p_t}{\int |\dot{m}|} \Big|_{outlet}. \quad (5)$$



Fig. 6. Location of control points at iteration design zero.

Of course, the largest heat exchange achieved better, but this is a secondary objective, being the pressure drop as the real cost function. In this section, an optimization process will be described to modify the shape of the fins according to the following objective:

- Minimize the pressure drop,  $\Delta p$ , between two planes before and after the fin location.
- Once the pressure drop is minimized during the optimization process, the heat exchange is monitored,  $\dot{Q}$ , between the fluid and the fin surfaces, in order to confirm that no strong variations were observed. To optimize this magnitude, the fin shape and the setup of the different fins will be studied. Apart from the fin shape on the XY plane, the additional geometrical degrees of freedom of the system analyzed are:
- The gap between fins,
  - the fin thickness.

We will split the global optimization process in two independent parts: first, we will perform a parametric study of the fin thicknesses and the distance between fins of the symmetric configuration (see Fig. 2), both directly related to the number of fins. Second, computing the periodic model (see Fig. 3), we will optimize the geometric design of the fin shape on the XY plane based on the adjoint method [41,42], using the pressure drop per lateral fin surface area  $\Delta p/A_{xy}$  as the objective function, which means that we will improve the aerodynamic design of the fin while the heat exchange is kept as constant as possible.

To perform the second part, the adjoint method is used. The adjoint method is an efficient process to predict the influence of input design geometry,  $\mathbf{D}$ , on some engineering cost function of interest,  $\mathbf{L}$ , which as we already said, in our case, is based on the pressure drop generated by the SACOC divided the lateral fin area,  $\Delta p/A_{xy}$ . The process is performed in two major steps. First, an steady state solution, also known as *primal solution*,  $\mathbf{Q}$ , is computed on an initial grid with control points  $\mathbf{X}^0$ . In the second step, the adjoint problem based on the previously numerical solution, is evaluated. This evaluation computes the sensitivities of the cost function with respect to the different design parameters:

$$\frac{d\mathbf{L}}{d\mathbf{D}} = \left[ \frac{\partial \mathbf{L}}{\partial \mathbf{X}} + \frac{\partial \mathbf{L}}{\partial \mathbf{Q}} \frac{\partial \mathbf{Q}}{\partial \mathbf{X}} \right] \frac{d\mathbf{X}}{d\mathbf{D}} \quad (6)$$

where  $\frac{d\mathbf{X}}{d\mathbf{D}}$  is the Jacobian matrix. The linear system created is solved by means of a GMRES algorithm. The cost of solving the linear system of equations is similar to solving the primal flow solution in terms of iterations and computational time. As result, the most sensitive zones of the geometry are detected on the grid points. The gradient of this sensitivity map indicates the movement of the grid points through the control points to obtain an optimized cost function. An example of the sensitivity map for the initial periodic configuration described will be illustrated in Section 4.3.3. The control points are moved according to the previous step of the optimization process, as a consequence the geometry and mesh are modified and a new iteration is performed until an optimized geometry is obtained (Fig. 6).

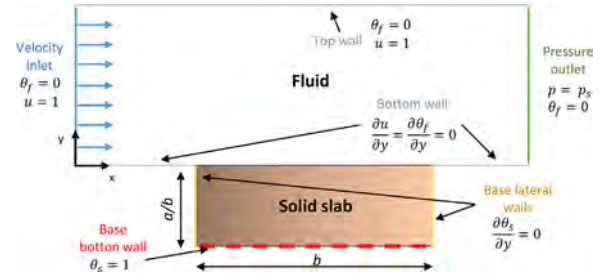


Fig. 7. Computational setup for the first 2D validation without fins V1 (based on Fig. 1 [15]).

This iterative process is finished when the variation of the cost function value is below a given tolerance.

### 3. Numerical verification and validation

In this section, two test cases are defined to verify and validate the computational tool. The two cases, named as  $V_1$  and  $V_2$ , are:

1.  $V_1$ : This verification computes a conjugate heat transfer problem for 2D flat plate (without fins) in turbulent regime. The Nusselt number and the temperature isolines will be compared to previously published solutions of the problem [15].
2.  $V_2$ : A 3D validation will be performed including the presence of the fins in the geometry. The case selected for comparison is presented in Kim et al. [34], where computational and experimental results are shown.

#### 3.1. $V_1$ : flat plate

For this verification without fins, a previous study by Vynnycky et al. [15], has been used as reference. In this work, the heat transfer associated with the forced convection flow over a rectangular conducting slab sited in an aligned uniform turbulent stream is investigated in 2D analytically and numerically. Both internal and external thermal conductivities are taken into consideration using a conjugate heat transfer model based on the full compressible Navier–Stokes equations and the heat equation for the slab.

##### 3.1.1. Setup

A schematic description of the modeled problem is given in Fig. 7. The fluid domain is rectangular with a height,  $H/b = 1$ , and length,  $L/b = 3$ . The conducting slab is defined by a height,  $a/b$ , and length,  $b$ . And the distance from the slab leading edge to the inlet boundary condition is  $x/b = 0.5$ .

We assume that the lower side of the slab  $y = -a/b$  is held at a uniform temperature  $\theta = 1$ , whilst the vertical boundaries of the slab are both insulated.

The ambient forced flow is characterized by a uniform velocity,  $U_\infty$ , and temperature,  $T_\infty$ . It is also assumed that in the fluid boundary upstream and downstream the slab the heat flux, the normal outflow and the viscous shear are zero. All lengths were

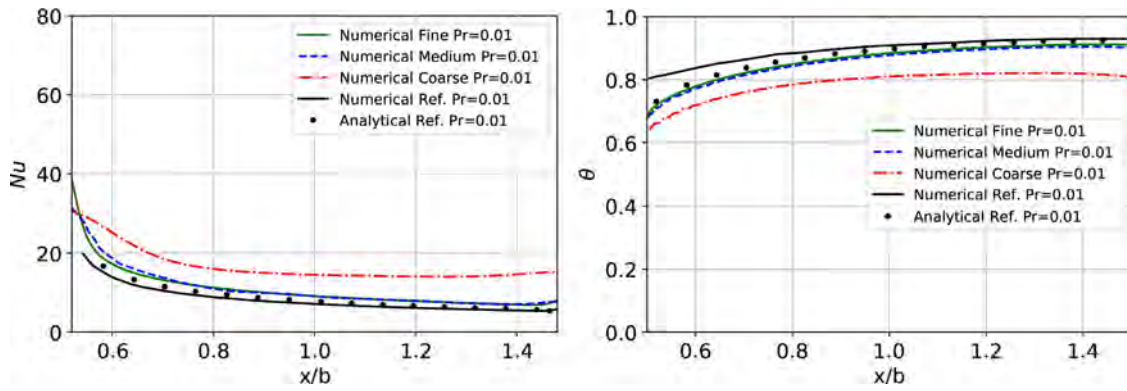


**Fig. 8.** Grid convergence study using a coarse, a medium and a fine grid compared with the reference work [15] for the local Nusselt number  $Nu$  (left) and Conjugate Boundary Temperature  $\theta$  (left) along the convective wall with  $Re = 10^4$ ,  $Pr = 0.01$ ,  $\kappa = 20$  and  $\lambda = 0.25$ .

non-dimensionalised with the slab length  $b$ , velocities with  $U_\infty$  and temperatures as explained in Section 2.2.

Regarding the domain spatial discretization, a hybrid mesh formed by structured elements for the fluid boundary layer and the slab, and unstructured elements for the upper part, is used. The boundary layer is fully resolved using  $y^+$  values below one.

This verification test was computed for  $Re = 10^4$ ,  $k = 20$ ,  $a/b = 0.25$  and two different Prandtl numbers,  $Pr = 0.01, 100$ . The results obtained were compared with numerical and analytical results from the reference work [15].

The efficiency of this problem can be quantified in terms of the local Nusselt number  $Nu(x)$ , defined on the top of the slab as:

$$Nu(x) = -\frac{\partial \theta_f}{\partial y} \Big|_{y=0} \quad 1/2 \leq x \leq 3/2. \quad (7)$$

The average Nusselt number is defined as:

$$\overline{Nu} = \int_{1/2}^{3/2} Nu(x) dx. \quad (8)$$

### 3.1.2. Grid convergence

First, a grid convergence test was performed for  $Pr = 0.01$  using three different grid resolutions. The number of elements for each grid are  $7.44 \times 10^3$  (Coarse),  $2.26 \times 10^4$  (Medium) and  $9.55 \times 10^4$  (Fine). Fig. 8 shows the mesh convergence process, consequently, the local Nusselt number,  $Nu$ , given by the Eq. (7), and the Conjugate Boundary Temperature,  $\theta$ , approximate the reference results [15] as the mesh quality is increased. A convergence analysis based on the infinity norm, not included here, gives an error  $\approx 1\%$  between the medium and fine grids. Once the grid convergence test is satisfied, the following results are computed with the finest grid.

### 3.1.3. Results

Fig. 9 compares the analytical and numerical values of the local Nusselt number,  $Nu$ , and the conjugate boundary temperature,  $\theta$ , along the convective wall. A good agreement between the reference results and those presented in this work is observed, providing a good approximation of the heat transfer dissipation with an accurate temperature distribution over the slab. In the reference work [15], there are no  $Nu$  analytical results available for the case  $Pr = 100$ .

Fig. 10 compares the isosurfaces of the conjugate boundary temperature,  $\theta$ , with  $\Delta\theta = 0.1$  for both configurations ( $Pr = 0.01$  and 100). The simulation presents a very good agreement when compared to the results from the reference work [15], being able to reproduce the thermal conductivity through both subdomains (fluid and solid). Notice how, for the lower  $Pr$  number, the thermal boundary layer is more developed in the fluid due to the high thermal conductivity. On the other hand, the simulation with  $Pr = 100$

shows a larger temperature gradient inside the slab, while in the fluid the temperature variation is confined to a thin boundary layer close to the slab surface.

To justify the small differences between the computed results and those presented in Vynnycky et al. [15], it is important to mention that in the referenced work the inflow is kept uniform from  $x/b = 0$  to  $x/b = 0.5$ . Consequently, the boundary layer is not developed and no viscous and heat transfer effects are considered for  $x/b > 0.5$ . This consideration explains the differences between the numerical results obtained by the preliminary computation performed by our results and the results found in Vynnycky et al. [15].

Additionally, it is important to mention that the thermal and viscous scales are proportional to the Prandtl number, being the thermal resolution required in the thermal boundary layer,  $T^+ = y^+ Pr$ . Therefore, in the simulation  $Pr = 100$ , the thermal resolution ( $T^+$ ) is more demanding than the viscous resolution  $y^+$ , it will require a  $y^+ = 0.01$  to obtain a  $T^+ = 1$  and to resolve correctly with more accuracy the thermal boundary layer. However, in an industrial context where the Prandtl number required is  $Pr \approx 0.71$  at standard conditions, the thermal resolution is less demanding than the viscous resolution. Therefore, ensuring  $y^+ < 1$  both the thermal and the viscous boundary layers will be numerically well resolved.

## 3.2. $V_2$ : 3D flat plate with fins

This second test case is inspired on the experiments performed by Jonsson and Moshfegh [43]. A straight channel model is used to examine the aero-thermal performance of a plate fin surface having a bypass passage. Several fin geometries were set inside the wind tunnel in Jonsson and Moshfegh [43], being the one with parallel plate fins the one selected for this validation. As result, the fundamental heat exchanger performance with a 3D turbulent flow under ideal conditions was examined.

### 3.2.1. Setup

As this second test case is inspired from an experimental paper [43], where the geometry is expressed in dimensional units, see Table 1.

These dimensions correspond to the fin-channel configuration with aspect ratios  $H_{FIN}/H = 0.33$  and  $WF/W = 0.84$  for the width and height respectively, see [43]. The number of fins is equal to nine and the tested heat sinks were milled in aluminum of thermal conductivity  $k_s = 200$  W/(m K).

The computation has been performed in the periodic configuration described in Section 2.1 (see Fig. 3), consequently only one fin will be considered in the computation. In Fig. 11 the domain is shown and the following boundary conditions are indicated: no-slip and conjugate heat transfer boundary conditions are applied

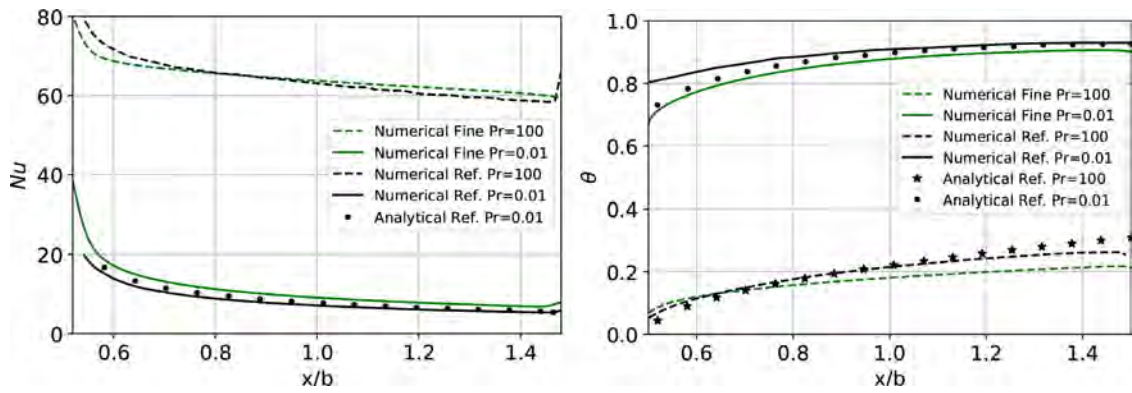


Fig. 9. Local Nusselt number  $Nu$  (left) and Conjugate Boundary Temperature  $\theta$  (right), compared with the reference work [15], at the convective wall with  $Re = 10^4$ ,  $Pr = 10^{-2}$ , 100,  $\kappa = 20$  and  $\lambda = 0.25$ .

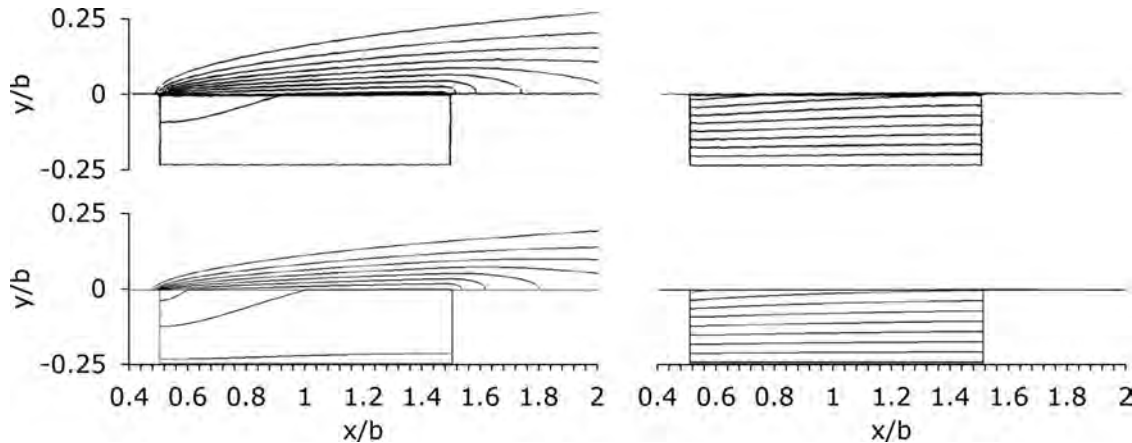


Fig. 10. Isosurfaces of conjugate boundary temperature ( $\Delta\theta=0.1$ ) of analytical [15] (top) and numerical (bottom) results with  $Pr = 0.01$ , 100 (right),  $Re = 10^4$ ,  $\kappa = 20$  and  $\lambda = 0.25$ .

Table 1

Geometrical dimensions of the wind channel and fins expressed in meters for the second test case, see [43].

Dimension	Notation	Length [m]
Channel length	L	0.2
Channel height	H	0.03
Channel width	W	0.0637
Fin base length	LFIN	0.0528
Fin height	HFIN	0.01
Separation between fins	SFIN	$5 \times 10^{-3}$
Fin thickness	WFIN	$1.5 \times 10^{-3}$
Fins width	WF	52.8
Distance leading edge Fin-Inlet	LU	0.025

Table 2

Geometrical dimensions of the wind channel, SACOC and fins expressed in meters.

Dimension	Notation	Length [m]
Channel length	L	$3 \times 10^{-1}$
Channel height	H	$1 \times 10^{-1}$
Channel width	W	$1 \times 10^{-1}$
Distance leading edge SACOC-Inlet	LU	$7.6 \times 10^{-2}$
Distance trailing edge SACOC-Outlet	LD	$3 \times 10^{-1}$
Fin height	HFIN	$2 \times 10^{-2}$
Fin base length	LFIN1	$1.25 \times 10^{-1}$
Fin top length	LFIN2	$1.05 \times 10^{-1}$
Separation between fins	SFIN	$2.175 \times 10^{-3}$
Fin thickness	WFIN	$1 \times 10^{-3}$
Fins width	WF	$4.9 \times 10^{-2}$
Fin base length	LB	$1.33 \times 10^{-1}$
Fin base height	HB	$1.5 \times 10^{-3}$
Fin base width	WB	$5.8 \times 10^{-2}$

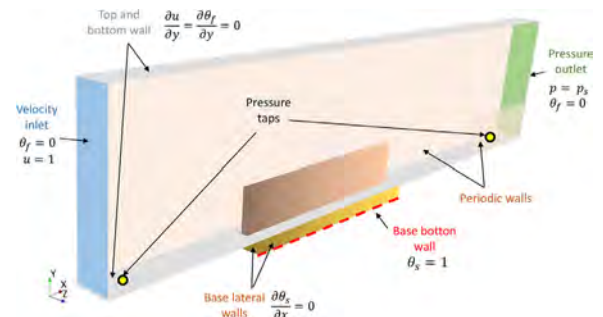


Fig. 11. Computational setup for the 3D validation case V2 with one fin and periodic boundary conditions.

on the fin walls; the velocity, temperature, turbulence kinetic energy and the dissipation rate of the turbulent kinetic energy is prescribed with a uniform distribution at the inlet, and static pressure is imposed at the outlet. The values of the boundary conditions for the turbulence variables  $k$  and  $\omega$  are given by Agonafer and Moffat [44]. Duct walls (top and bottom) are modeled as adiabatic walls with no-slip boundary conditions.

Regarding the grid structure, a fine hybrid mesh formed by structured elements for the fluid boundary layer and the slab, and unstructured elements for the upper part, with  $5.8 \times 10^5$  elements is used. The boundary layer is fully resolved using  $y^+$  values below one. A convergence analysis, not included here, shows a good compromise between accuracy and computational cost for this mesh.

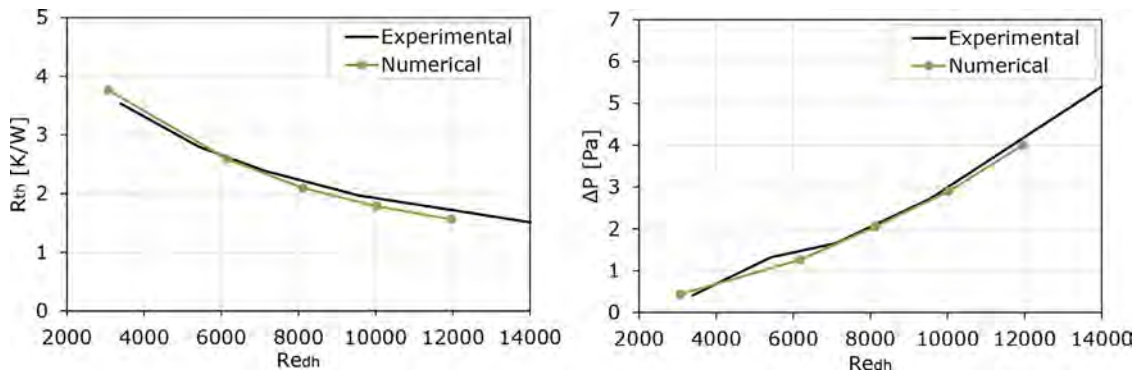


Fig. 12. Pressure drop,  $\Delta p$ , (left) and thermal resistance,  $R_{th}$ , (right) for the second validation case,  $V_2$ , at different Reynolds numbers. Experimental values are obtained from [43].

The Reynolds number is defined as  $Re = \frac{wd_h}{\nu}$ , where the reference length is the hydraulic diameter of the wind tunnel,  $d_h = \frac{2 \cdot H \cdot W}{H+W}$ . And the average air velocity is  $w = \frac{V}{A-A_{yz}}$ , where  $V$  is the volumetric air flow rate,  $A = H \cdot W$  is the wind tunnel cross sectional area and  $A_{yz} = 1.35 \times 10^{-4} \text{ m}^2$  is the fin frontal area. In our case, the Reynolds number range is  $4000 < Re_{d_h} < 14,000$  and the Prandtl is  $Pr = 0.764$ . In this case, due to the reduced velocities, the compressibility effects in the fluid are negligible.

The problem can be analyzed by the contour of the thermal resistance,  $R_{th}$ , defined as:

$$R_{th} = \frac{\Delta T}{\dot{Q}}, \tag{9}$$

where  $\dot{Q}$  is the heat exchange and  $\Delta T = T_c - T_\infty$  is the temperature difference between the heated wall base and the inflow.

Finally, in terms of aerodynamic penalties, the pressure drop,  $\Delta p$ , is measured using two pressure taps positioned over the flat plate in the center line with a distance,  $d$ , upstream and downstream of the fin respectively.

### 3.2.2. Results

The experimental measurements available were performed on the central fin where the flow and heat transfer process are considered insensitive to the presence of the lateral walls of the wind tunnel. The pressure drop over the heat sink was measured using two pressure taps positioned over the flat plate in the center line ( $Z = 0 \text{ m}$ ) a distance  $d = 0.05 \text{ m}$  upstream ( $X = 0.0038 \text{ m}$ ) and downstream ( $X = 0.1628 \text{ m}$ ) of the heat sink respectively. The pressure drop  $\Delta p$  and the thermal resistance  $R_{th}$  are both compared to the experimental measurements in Fig. 12. As can be observed, a good agreement is obtained between the computed values and the experimental measurements.

## 4. SACOC optimization

In this section, we will apply the optimization process described in Section 2.4 to the SACOC problem. As explained in Section 2.4, the process is divided in two independent tasks. First, the symmetry model is used (see Fig. 2) to investigate the fin thickness and separation effects. Second, the periodic model (see Fig. 3) is used with the adjoint method to optimize the fin shape on the XY plane. Before the explanation of the optimization process, the simulation setup and the grid convergence process are presented.

### 4.1. Setup

As the geometry of this final case is inspired by future experimental campaigns, similarly to the previous case in Section 3.2,

Table 3

Location of measurements sections.

Section	X [m]
UMS1	0
DMS1	0.25
DMS2	0.4
DMS3	0.5

Table 4

Air and Aluminium physical properties.

Property	Air	Aluminium
Density, [kg/m <sup>3</sup> ]	1.225	2702
Specific heat [J/kg K]	1004.9	896.0
Thermal conductivity [W/m K]	0.024	150

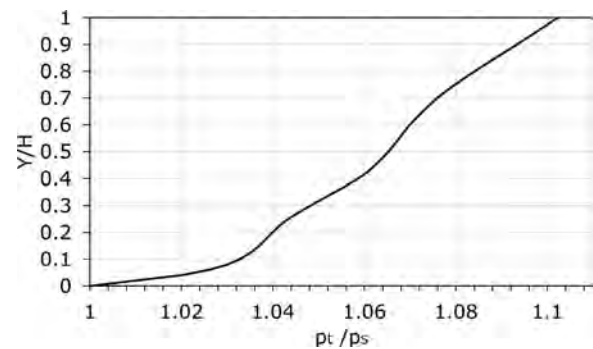


Fig. 13. Experimental non-dimensionalized total pressure profile at the inflow boundary. Pressure data provided by the aircraft engine company SAFRAN.

this case will also be expressed in dimensional units except for the inflow pressure profile and the classical non-dimensional numbers such as the skin friction, the conjugate temperature and the Reynolds and Mach numbers.

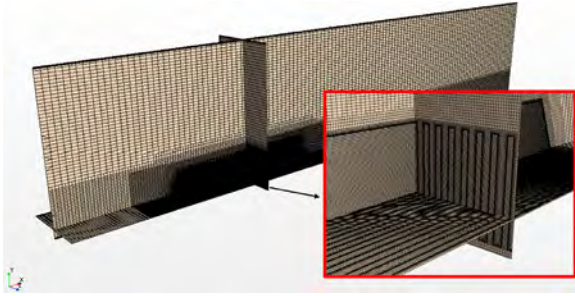
The setup was introduced in Section 2.1 and illustrated in Figs. 2 and 4, and the geometric dimensions are listed in Table 2. Additionally, Table 3 contains the four streamwise coordinates  $x$  of the measurement sections used in this work during the numerical analysis (see Fig. 2), and Table 4 contains the values of the fluid and solid properties.

For the inflow boundary conditions, an experimentally measured inflow total pressure profile is imposed (see Fig. 13), where the pressure data were provided by the aircraft engine company SAFRAN. The complementary turbulence inflow values are 5% for the turbulent intensity and 10% for the turbulent viscosity ratio.

**Table 5**

Mesh convergence study. Six different meshes with different characteristic mesh size  $H_c$  and grid size inside the fin. The pressure loss  $\Delta p$  and the heat transfer  $\dot{Q}/\text{NFIN}$  are monitored.

Grid	$H_c$ [mm]	$H_{fin}$ [mm]	Grid cells	$\Delta p$ [Pa]	$\dot{Q}/\text{NFIN}$ [W]
1	12	0.5	$5.01 \times 10^5$	909.51	85.12
2	8	0.5	$1.06 \times 10^6$	844.92	88.04
3	4	0.5	$2.80 \times 10^6$	796.01	95.07
4	2	0.5	$1.14 \times 10^7$	731.40	95.47
5	2	0.25	$1.31 \times 10^7$	732.70	95.43
6	2	0.125	$2.36 \times 10^7$	733.35	95.47

**Fig. 14.** Global perspective of grid number 5 (top), details of the fin zone (bottom).

For the outflow, the pressure outlet value is fixed to  $p_s = 122,364$  Pa. Finally, the temperature difference between the bottom heated aluminium fins and the inflow is  $\Delta T = 100$  K, being  $T_\infty = 300$  K and  $T_c = 400$  K. Regarding the fluid and solid properties, Table 4 depicts these values. Besides, the dynamic viscosity is calculated through the Shutterland's law[45].

In contrast to the previous validation cases, the dominant non-dimensional numbers such as the Reynolds  $Re = 2 \times 10^6$  and Mach  $M \approx 0.5$  numbers are high enough that the compressible and turbulent effects should be taken into account.

In this section, the pressure drop is computed using the Eq. (5) as the mass-flow averaged absolute total pressure difference between the inlet and outlet sections.

The local heat transfer coefficient  $h$  and the skin friction coefficient  $C_f$  are defined as:

$$h = \frac{1}{T_c - T_{ref}} k \left. \frac{\partial T}{\partial n} \right|_{A_f}, \quad C_f = \frac{1}{\frac{1}{2} \rho U_\infty^2} \mu \left. \frac{\partial u}{\partial n} \right|_{A_f}, \quad (10)$$

where the reference temperature  $T_{ref}$  is the one that satisfies the equation of state for both the outflow static pressure  $P_s$  and inflow density  $\rho_\infty$ , and the total heat transfer coefficient  $h_g$  is the integral of the local heat transfer coefficient on the fin area  $A_f$ .

#### 4.2. Grid convergence

Using one half of the geometry (symmetric model), a grid convergence process based on the pressure loss  $\Delta p$  (see Eq. (5)) and the heat transfer per fin  $\dot{Q}/\text{NFIN}$  for seven different meshes is performed. All meshes are designed using a minimum grid thickness of  $2.0 \times 10^{-6}$  mm, which implies  $y^+ \sim 0.5$  for the boundary layers. The mesh convergence process is summarized in Table 5, where the first column is the characteristic mesh size  $H_c$  close to the wall fin, and the second is the grid size inside the fins,  $H_{fin}$ , see Fig. 14.

Notice that the grid refinement can be divided in two parts: the fluid refinement (Grids #1, #2, #3 and #4) and the solid refinement (Grids #4, #5 and #6). Regarding the fluid refinement, notice how the error between the different grids is reduced to 3.5% between grids #3 and #4. Finally, in the solid refinement, very small differences were found between the grids #4, #5 and #6 where the refinement inside the fins has little influence, show-

**Table 6**

Pressure drop  $\Delta p$ , heat transfer per fin and the total heat transfer  $\dot{Q}$  when the separation between fins and the number of fins is varied inside the fins width distance WF. The middle case NFINS = 16 is used as reference case to compute the variations.

SFIN/WFIN	NFINS	$\Delta p$ [Pa]	$\dot{Q}/\text{NFIN}$ [W]	$\dot{Q}$ [W]
1.0875	24	807.2 (+10.1%)	74.98 (-21.4%)	1799.5 (+17.8%)
2.175	16	732.7 (0%)	95.43 (0%)	1526.9 (0%)
4.292	10	667.2 (-8.9%)	104.4 (+9.4%)	1044.2 (-31.6%)

**Table 7**

Pressure drop  $\Delta p$ , heat transfer per fin and the total heat transfer  $\dot{Q}$  when the fin thickness and the number of fins is varied inside the fins width distance WF. The middle case NFINS = 16 is used as reference case to compute the variations.

WFIN [mm]	NFINS	$\Delta p$ [Pa]	$\dot{Q}/\text{NFINS}$ [W]	$\dot{Q}$ [W]
0.647	18	737.2 (+0.6%)	73.09 (-23.4%)	1315.5 (-13.8%)
1	16	732.7 (0%)	95.43 (0%)	1526.9 (0%)
1.45	14	748.3 (+2.2%)	108.13 (+13.3%)	1513.8 (-0.8%)

ing less than 0.2% variation. Therefore, balancing the computational load and the accuracy demand, the final grid selected for the optimization process is grid number #5, that contains  $1.31 \times 10^7$  cells, where  $1.19 \times 10^7$  are for the fluid part and  $1.20 \times 10^6$  cells are for the solid part, see Fig. 14.

#### 4.3. Shape and setup optimization.

##### 4.3.1. Separation between fins effect

The effect of the separation between fins is studied in this section. As part of the first task, we define the reference setup with 16 fins and dimensions according to Table 2.

Keeping the fin base length LFIN1 and the fin thickness WFIN constant and varying the distance between fins SFIN from  $1.08 \times 10^{-3}$  m to  $4.29 \times 10^{-3}$  m and consequently the number of fins NFIN. We computationally confirmed, using a medium grid that reduces the size between fins and consequently includes a larger number of fins in the WF length:

1. The pressure drop,  $\Delta p$ , and the total heat transfer,  $\dot{Q}$ , are both increased as expected (see Fig. 15).
2. The heat transfer per fin,  $\dot{Q}/\text{NFINS}$ , decreases (see Table 6).

Reducing the distance between fins, which reduces the free flow area, the velocity increases within the fins. However, it does mean a higher heat transfer. This effect is shown in Fig. 16 with the local heat transfer coefficient  $h$  and skin friction coefficient. The results have shown how reducing the distance between fins produces a flow constrain within the fins that reduces the heat transfer efficiency. Additionally, note how the flow is accelerated locally in the lower part of the leading edge induced by the geometry angle. It is directly related to the increasing of heat transfer and skin friction.

##### 4.3.2. Fin thickness effect

The second step of the analysis was performed keeping the horizontal length occupied by the fins WF, the fin base length LFIN1 and the distance between fins SFIN constant and varying the fin thickness WFIN between  $0.65 \times 10^{-3}$  m and  $1.45 \times 10^{-3}$  m and consequently the number of fins NFIN. We computationally confirmed, using a medium grid, that decreasing the fin thickness and consequently increasing the number of fins in the WF length, the pressure drop  $\Delta p$  remains almost constant and the heat transfer per fins decreases (see Table 7). However, this increasing of fins number, could compensate the loose of heat transfer per fin. Therefore, a local maximum is found for the total heat transfer  $\dot{Q}$  when the WFIN =  $1 \times 10^{-3}$  m (see Fig. 17). As in the previous test varying the distance between fins, the heat transfer per fin  $\dot{Q}/\text{NFINS}$  increases when the fin thickness is increased.

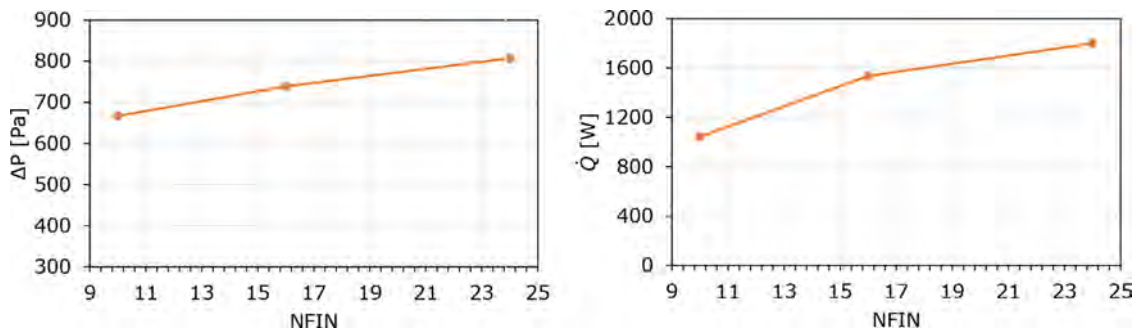


Fig. 15. Pressure drop,  $\Delta p$ , (left) and the total heat transfer,  $h$ , (right) when the separation between fins and the number of fins is varied with a fixed fins width distance WF.

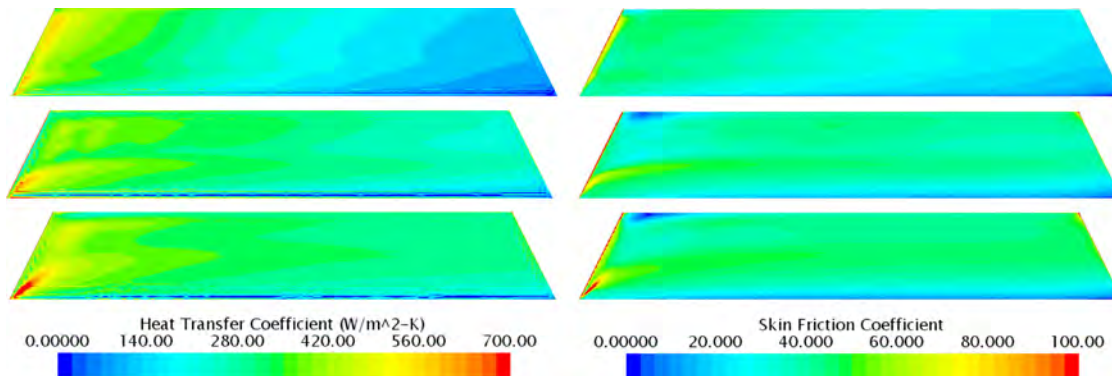


Fig. 16. Heat transfer coefficient (left) and skin friction coefficient (right) with three different separation between fins: SFIN/WFIN = 1.0875 (top), 2.175 (middle) and 4.292 (bottom).

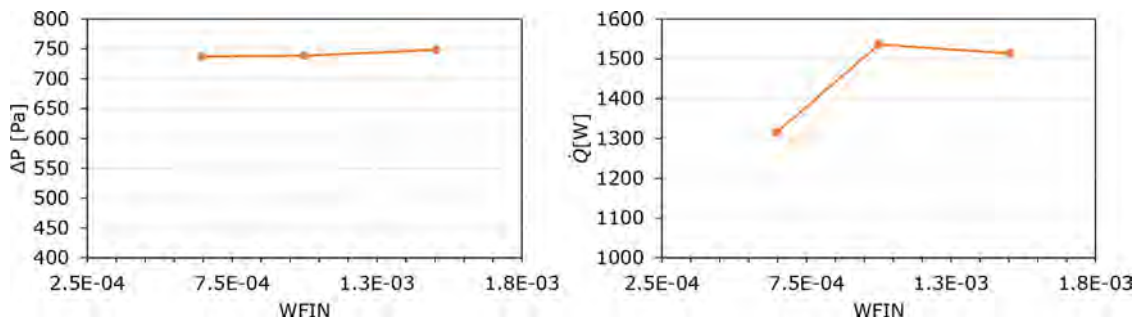


Fig. 17. Pressure drop  $\Delta p$ , heat transfer per fin and the total heat transfer  $h$  when the fin thickness and the number of fins is varied inside the fins width distance WF.

In contrast to the previous Section 4.3.1, Fig. 18 depicts how the shear stress distribution barely changes in the three different configurations when the separation between fins is constant. However, the heat transfer increases proportionally to the fin thickness as the addition of material permits a higher heat transfer.

#### 4.3.3. Shape optimization of the periodic case

Finally, as part of the last task, Fig. 19 depicts the vector displacements obtained from the sensitivity computation on the control points and used to modify the SACOC geometry at the iteration design zero. Notice that we use the periodic model (see Fig. 3) according the values of Table 1.

Then, Table 8 shows the iterations of the process, where the control points adjust the optimal shape of the fin. The final geometry Mod 5 presents a lateral area,  $A_{xy}$ , increase of 8.6% compared to the original design, but showing a pressure drop reduction of 74 Pa (11.6%). Despite the iterative lateral area growth, the total heat transfer  $h$  is only reduced in 0.5 W (0.5%). Besides, the evolution of the pressure drop and heat transfer coefficient during the iterations of the optimization process is presented in Fig. 20.

Table 8

The lateral fin area,  $A_{xy}$ , the pressure drop,  $\Delta p$ , and the total heat transfer,  $\dot{Q}$ , during the different iterations indicated by the Adjoint optimization process.

Geometry	$A_{xy}$ [m <sup>2</sup> ]	$\Delta p$ [Pa]	$\dot{Q}$ [W]
Original	$2.30 \times 10^{-3}$	636.4	95.2
Mod 1	$2.30 \times 10^{-3}$	619.7	95.3
Mod 2	$2.35 \times 10^{-3}$	586.2	95.3
Mod 3	$2.38 \times 10^{-3}$	575.1	95.2
Mod 4	$2.43 \times 10^{-3}$	564.6	94.7
Mod 5	$2.50 \times 10^{-3}$	562.4	94.7

The comparison between the final geometry of the fin obtained after the optimization process and the original one is shown in Fig. 21. Notice how the shape of the optimized geometry eliminates the sharp corners and smooths the perimeter of the fin. It is also relevant that the bow shows a prominent bulb shape that moves upwards and upstream the high pressure point, which optimizes the aerodynamic performance.

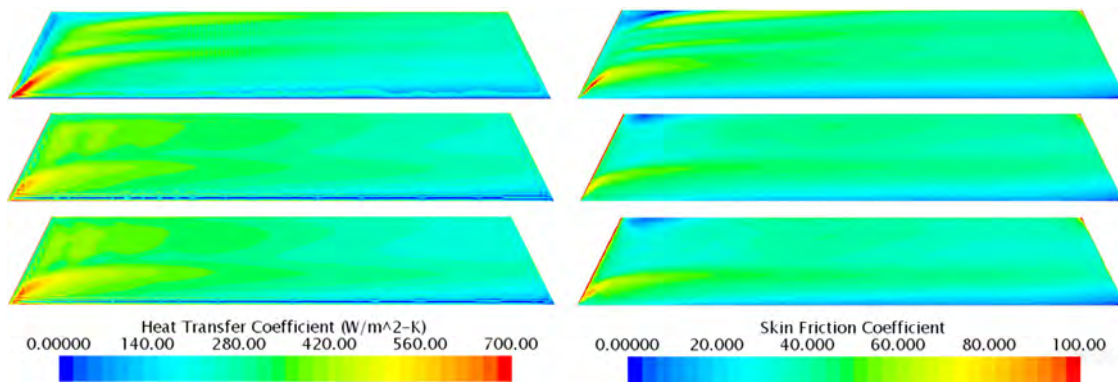


Fig. 18. Local heat transfer coefficient (left) and skin friction coefficient (right) with three different separation between fins:  $W_{FIN} = 0.647$  mm (top), 1.0 mm (middle) and 1.45 mm (bottom).

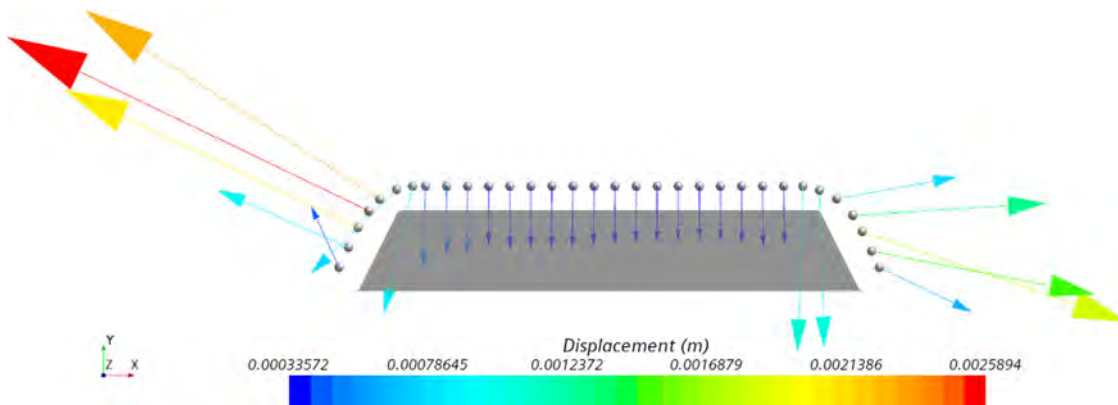


Fig. 19. Vector displacement on control points at the iteration design zero.

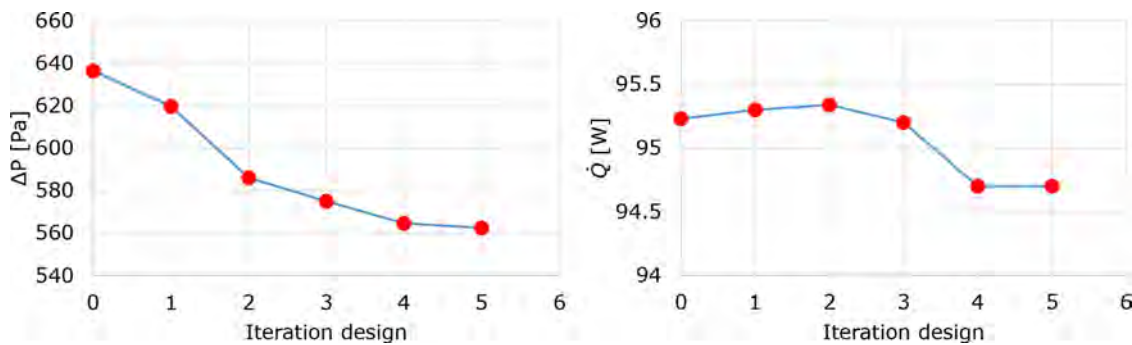


Fig. 20. Evolution of the pressure drop (left) and the total heat transfer (right) for the different optimized designs.



Fig. 21. Comparison between the original fin shape and the fourth and fifth iterations Mod 4 and 5.

To answer the question of how much depends this method on the mesh, the last two design iterations (Mod 4 and Mod 5) have been computed with an additional finer mesh. This finer grid is based on the refinement values of the grid number 6 (see Table 5). The results are very similar when compared to the original mesh (Grid 5), concluding that the mesh has a small influence on this shape optimization process. See Table 9 for comparison between the different meshes.

As can be observed, the difference between the thermal and aerodynamic results obtained for the two different meshes (5 and

6) show that the optimization process has little mesh dependence. When the optimized geometry is compared to the original case, the pressure drop variation is between 10% and 11% and the heat transfer variation below 2%.

#### 4.4. Results for the optimized SACOC.

As the main objective of the optimization process is to decrease the pressure drop caused by the SACOC presence losing minimum heat exchange. This statement comes from the experience achieved by the aircraft engine industry. We obtained an optimized shape attending this requirement applying the adjoint method. Additionally, the distance between fins and the fin thickness effect is analyzed (see Figs. 15 and 17) and some comments are required. Fig. 15, expresses that both the pressure drop and the heat transfer are proportional to the number of fins, then if no additional heat transfer is required, the number of fins should remain as 16. Re-

**Table 9**  
Comparison of the pressure drop  $\Delta p$  and the total heat transferred power  $\dot{Q}$  during the different iterations indicated by the Adjoint optimization process for two different meshes. Grids 5(original) and 6 (finer) are detailed in Table 5.

Geometry	$\Delta p$ [Pa]			$\dot{Q}$ [W]		
	Grid 5	Grid 6	Difference [%]	Grid 5	Grid 6	Difference [%]
Original	636.4	633.3	-0.49	95.2	96.9	1.75
Mod 4	564.6	569.4	0.84	94.7	96.0	1.35
Mod 5	562.4	560.2	-0.39	94.7	95.0	0.31

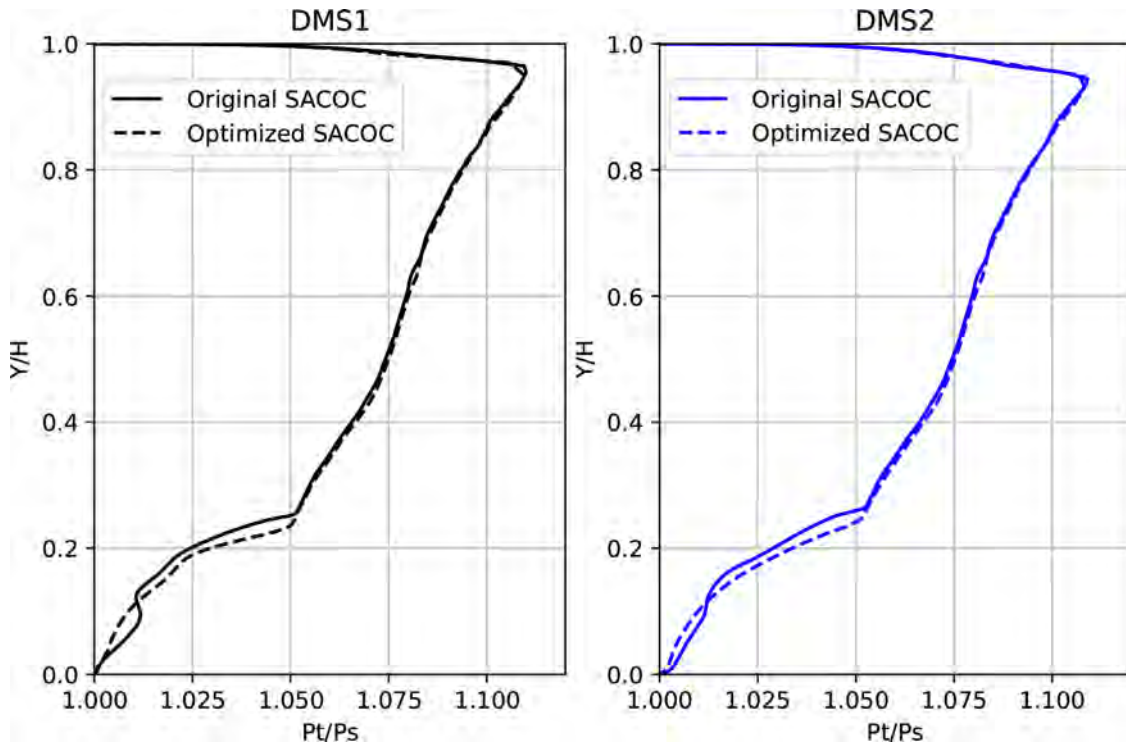


**Fig. 22.** Comparison of the pressure profiles when the SACOC contains the original fins and when they are replaced by the optimized fins at the positions DMS1 and DMS2.

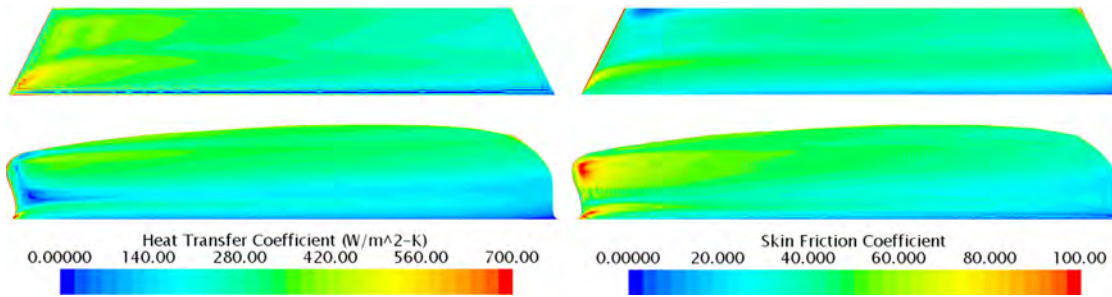


**Fig. 23.** Local heat transfer coefficient (left) and skin friction coefficient (right) with reference (top) and optimized (bottom) geometry.

Regarding the fin thickness, we should mention that the optimum heat transfer was obtained for the thickness used in the design case where the pressure drop does not suffer relevant variations (see Fig. 17). As consequence, the optimum design in terms of number of fins and fin thickness is the one already presented as the design case. However, these results give useful information for alternative designs of the geometry based on new requirements.

For the sake of completeness, in this section the fins of the particular setup described in Section 4.2 are replaced by the ones obtained after the optimization process performed in Section 4.3 where the number of fins and the fin thickness is the same in both configurations. After the shape optimization, a pres-

sure drop of 77.6 Pa (10.6%) is obtained, while the heat transfer per fin and the total heat transfer both vary less than 0.3%. In Fig. 22 the pressure profile between the case with the original fins and the optimized ones is presented. As can be appreciated in the fin area at the bottom part of the figure, the pressure profiles are clearly modified for the test positions DMS1 and DMS2 downstream the SACOC, where the flow is accelerated.

Again, Fig. 23 compares both designs in terms of heat transfer and skin friction coefficients along the fin and shows the areas with highest heat transfer. In the optimized shape, this area is located at the bulb of the leading edge. Besides, Fig. 24 shows the conjugate boundary temperature contour for both the fluid and

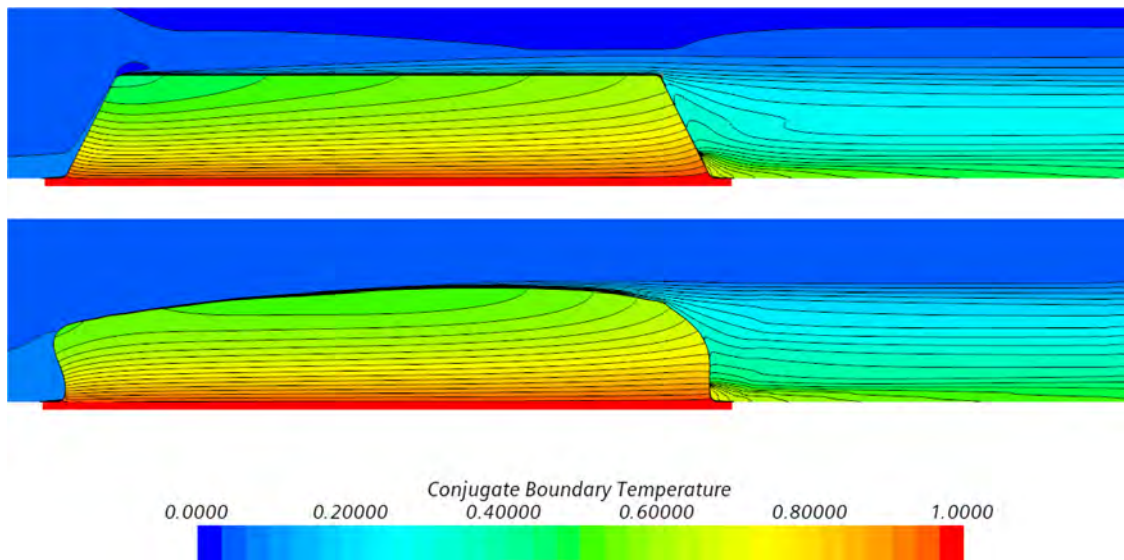


Fig. 24. Comparison of the non-dimensional temperature field between the original design (top) and the one obtained after the fourth iteration Mod 4 for the fine mesh (bottom).

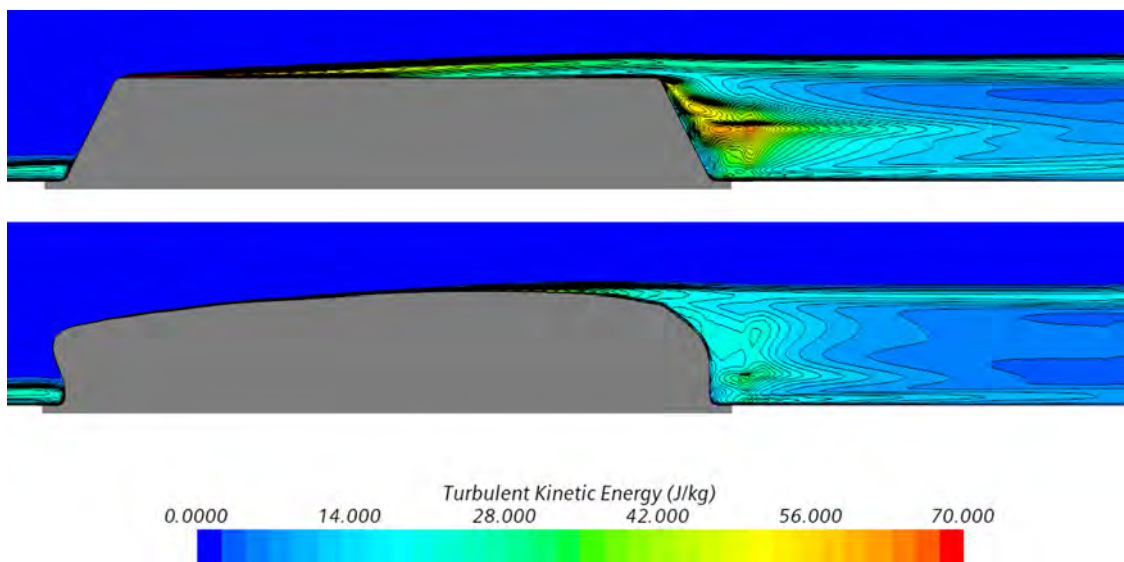


Fig. 25. Comparison of the turbulent kinetic field between the original design and the one obtained after the fourth iteration Mod 4 for the fine mesh.

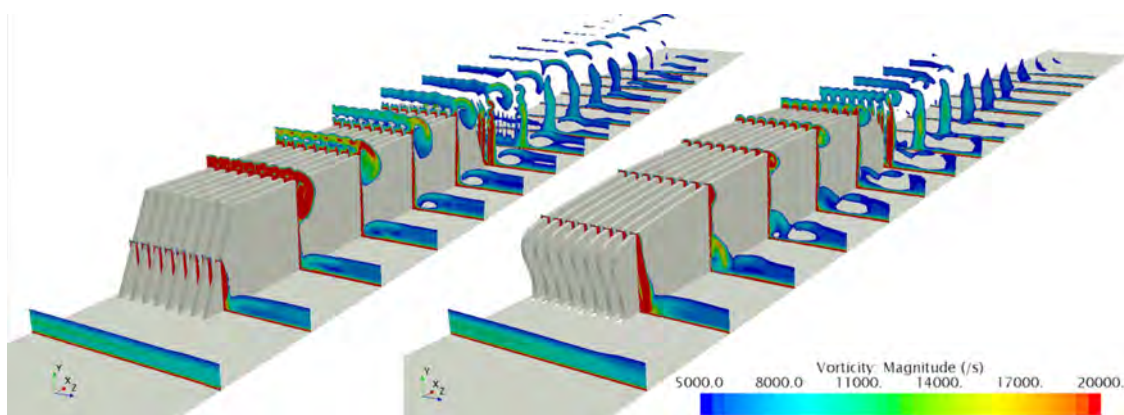


Fig. 26. Comparison of the vorticity profiles when the SACOC contains the original fins and when they are replaced by the optimized fins at different YZ sections along x-direction.

solid. The thermal wake and the temperature distribution on the fin are similar in both cases, resulting a very similar heat transfer.

Finally, regarding the aerodynamics, Figs. 25 and 26 depict a comparison of the flow pattern downstream and around the fins respectively. Fig. 25 shows how the turbulent kinetic energy is reduced with the optimized SACOC. Comparing both wakes, in the reference model the flow is detached by the sharp corner present at the leading edge, while in the optimized SACOC the detachment occurs past the middle of the fin with less production of turbulent kinetic energy.

In Fig. 26 a contour plot of the vorticity magnitude is represented for different sections along the  $x$ -direction for both designs. We can observe that the size and evolution of the primary vortex created at the top of the external fin presents significant differences in both cases. Note how the primary vortex is reduced in the optimized model producing a wake with less vorticity intensity.

## 5. Conclusions

In this work we have presented an efficient numerical methodology to optimize the global performance of a SACOC. This optimization process requires the definition of an objective, which in our case was given by the industry, according to which the new SACOC design should minimize the pressure drop between the inflow and outflow sections but keeping the heat transfer similar to the original case. The optimization methodology presented was split in two parts: first, the optimal setup in terms of fin thickness and distance between fins for a given SACOC width is also studied by parametric variation. Second, the fin shape was optimized using an adjoint method, where several control points refined the fin geometry according to the gradient of the sensitivity function computed. Once the optimal geometry is defined, a validated and efficient numerical method solves the conjugate heat transfer problem coupling the Reynolds averaged compressible Navier–Stokes equations with the heat transfer equation for the solid fins. The final result, when the optimized geometry is used, presents a substantial pressure drop reduction 10.6% with a negligible heat transfer variation. The CFD methodology used permits a complete comparison of skin friction coefficient and the heat transfer coefficient than explains both the pressure reduction and the heat transfer conservation.

## Declaration of Competing Interest

The authors declare that they have no known competing financial interests or personal relationships that could have appeared to influence the work reported in this paper.

## CRediT authorship contribution statement

**Miguel Chávez-Modena:** Conceptualization, Methodology, Software, Validation, Formal analysis, Investigation, Resources, Writing – review & editing, Visualization. **Leo Miguel González:** Conceptualization, Methodology, Formal analysis, Investigation, Resources, Writing – original draft, Writing – review & editing, Supervision. **Eusebio Valero:** Conceptualization, Formal analysis, Writing – review & editing, Supervision, Project administration, Funding acquisition.

## Acknowledgements

This project has received funding from the Clean Sky 2 Joint Undertaking under the European Union's Horizon 2020 research and innovation programme under grant agreement no. 831977 Leo M. González acknowledges the financial support from the Spanish Ministry for Science, Innovation and Universities (MCIU) under

grant RTI2018-096791-B-C21. The authors acknowledge the computer resources and technical assistance provided by the Centro de Supercomputación y Visualización de Madrid (CeSViMa). The authors also wish to thank Safran Aircraft Engines for their kind permission to share the data presented in this publication.

## References

- [1] D. Reay, C. Ramshaw, A. Harvey, *Process Intensification: Engineering for Efficiency, Sustainability and Flexibility*, Butterworth-Heinemann, Oxford, 2013.
- [2] J. Rishmany, C. Mabru, R. Chieragatti, F.R. Aria, Simplified modelling of the behaviour of 3D-periodic structures such as aircraft heat exchangers, *Int. J. Mech. Sci.* 50(6) (2008) 1114e22.
- [3] J. Griffin, D. Singer, L. Summers, Lubrication cooling system for aircraft engine accessory, U.S. Patent No. 4,151,710 (2008).
- [4] J. Sousa, L. Villafane, G. Paniagua, Thermal analysis and modeling of surface heat exchangers operating in the transonic regime, *Energy* 64 (2014) 961–969.
- [5] H. Iwasaki, T. Sasaki, M. Ishizuka, Cooling performance of plate fins for multi-chip modules, *IEEE Trans. Compon., Pack., Manuf. Technol.* 18 (1995) 144–147.
- [6] D. Gonzalez Cuadrado, A. Marconnet, G. Paniagua, Inverse conduction heat transfer and Kriging interpolation applied to temperature sensor location in microchips, *J. Electron. Packag.* 140 (2018) 1–8.
- [7] D. Bajusz, A. Cornet, J. Friedel, N. Raimarckers, Air-oil heat exchanger placed at the location of the air separator nose of a turbojet, and a turbojet including such an air-oil heat exchanger, TechSpace Aero S.A., Milmort (BE), US Patent 2009/0165995A1 (2009).
- [8] B. Olver, A. Ciampa, R. Marrano, R. Trepanier, S. Lamarre, M. Bernard, P. Germain, Turbofan bypass duct air cooled fluid cooler installation, Pratt & Whitney Canada Corp. (CA), US Patent 2008/0053059 A1 (2008).
- [9] E. Elovic, Cooling air cooler for a gas turbofan engine, General Electric Company, Cincinnati, Ohio (US), US Patent 004254618 (1981).
- [10] J. Elder, Gas turbine engine heat exchanger with tapered fins, Hamilton Sundstrand Corporation, US Patent 8784047 B2 (2010).
- [11] C. Zähringer, K. Stastny, S. Ardey, Towards the powerhouse for more electric aircraft-dedicated engine concepts, in: *Proceedings in 19th International Symposium on Air Breathing Engines (ISABE)*, 2009.
- [12] H. Streifinger, Fuel/oil system thermal management in aircraft turbine engines, RTO-Applied Vehicle Technology Panel, Symposium on Design Principles and Methods for Aircraft Gas Turbine Engines, Toulouse, France, 1998.
- [13] M. Flouros, H. Streifinger, Lubrication systems for aircraft gas turbines engines, new component developments for future applications, *Lubrication Systems for Aircraft Gas Turbine Engines*, Biarritz, France, 2012.
- [14] T.L. Perelman, On conjugated problems of heat transfer, *Int. J. Heat Mass Transf.* 3 (1961) 293–303.
- [15] M. Vynnycky, S. Kimura, K. Kanev, Forced convection heat transfer from a flat plate: the conjugate problem, *Int. J. Heat Mass Transf.* 41 (1) (1998) 45–59.
- [16] E.M. Sparrow, B.R. Baliga, S.V. Patankar, Forced convection heat transfer from a shrouded fin array with and without tip clearance, *J. Heat Transf.* 100 (1978) 572–579.
- [17] E.M. Sparrow, T.J. Beckey, Pressure drop characteristics for a shrouded longitudinal-fin array with tip clearance, *J. Heat Transf.* 103 (1981) 393–395.
- [18] E.M. Sparrow, D.S. Kadle, Effect of tip-to-shroud clearance on turbulent heat transfer from a shrouded, longitudinal fin array, *J. Heat Transf.* 108 (1986) 519–524.
- [19] K.S. Lau, R.L. Mahajan, Effects of tip clearance and fin density on the performance of heat sinks for vlsi packages, *IEEE Trans. Compon. Hybrids, Manuf. Technol.* 12 (1989) 756–765.
- [20] R.A. Wirtz, W. Chen, Longitudinal fin heat sink performance in arrays of low-profile electronic packages, *Adv. Electron. Packag.* 58 (1993) 809–817.
- [21] R.A. Wirtz, W. Chen, R. Zhou, Effect of flow bypass on the performance of longitudinal fin heat sinks, *ASME J. Electron. Packag.* 116 (1994) 206–211.
- [22] D.S. Kadle, E.M. Sparrow, Numerical and experimental study of turbulent heat transfer and fluid flow in longitudinal fin arrays, *J. Heat Transf.* 108 (1986) 16–23.
- [23] Y. Sata, H. Iwasaki, M. Ishizuka, Development of prediction technique for cooling performance of finned heat sink in uniform flow, in: *Proc. 1996 InterSoc. Conf. Thermal Phenom. Electron. Syst.*, 1996, pp. 108–114.
- [24] H. Jonsson, B. Moshfegh, Influence of fin spacing, fin thickness, and inlet velocity on the performance of plate fin heat sinks under varying bypass conditions using CFD, *Int. J. Heat Exch.* 1 (2) (2000) 177–196.
- [25] H. Jonsson, B. Moshfegh, Modeling and characterization of plate fin heat sinks under bypass flow conditions using computational fluid dynamics methods, *IEEE Trans. Compon. Packag. Technol.* 24 (2) (2001) 142–149.
- [26] H. Iwasaki, T. Sasaki, M. Ishizuka, Cooling performance of plate fins for multi-chip modules, in: *Proc. 1994 InterSoc. Conf. Thermal Phenom. Electron. Syst.*, 1994, pp. 144–147.
- [27] E.M. Sparrow, B.R. Baliga, S.V. Patankar, Heat transfer and fluid flow analysis of interrupted-wall channels, with application to heat exchangers, *J. Heat Transf.* 99 (1977) 4–11.
- [28] E.M. Sparrow, C.H. Liu, Heat-transfer, pressure-drop and performance relationships for in-line, staggered, and continuous plate heat exchangers, *Int. J. Heat Mass Transf.* 22 (1979) 1613–1625.

- [29] B. Boesmans, F. Christiaens, J. Berghmans, E. Beyne, Design of an optimal heat-sink geometry for forced convection air cooling of multi-chip modules, in: Proc. Eurotherm Seminar 29 Thermal Manag. of Electron. Syst., 1993, pp. 267–276.
- [30] C.L. Chapman, S. Lee, B.L. Schmidt, Thermal performance of an elliptical pin fin heat sink, in: Proc. 10th IEEE Semi-Therm Symp., 1994, pp. 24–31.
- [31] P. Sathyamurthy, P.W. Runstadler, S. Lee, Numerical and experimental evaluation of planar and staggered heat sinks, in: Proc. InterSoc. Conf. Thermal Phenom. Electron. Syst., 1996, pp. 132–139.
- [32] J. Min, J. Jeong, M. Ha, K. Kim, High temperature heat exchanger studies for applications to gas turbines, *Heat Mass Transf.* 46 (2009) 175–186.
- [33] S. Kim, J. Min, M. Ha, C. Son, Investigation of high-speed bypass effect on the performance of the surface air-oil heat exchanger for an aero engine, *Int. J. Heat Mass Transf.* 77 (2014) 321–334.
- [34] M. Kim, M.Y. Ha, J.K. Min, A numerical study on various pin-fin shaped surface air-oil heat exchangers for an aero gas-turbine engine, *Int. J. Heat Mass Transf.* 93 (2016) 637–652.
- [35] L. Villafañe, G. Paniagua, Aerodynamic impact of finned heat exchangers on transonic flows, *Exp. Therm. Fluid Sci.* 97 (2018) 223–236.
- [36] K. Morimoto, H. Kinoshita, Y. Suzuki, Adjoint analyses of enhanced solidification for shape optimization in conjugate heat transfer problem, in: APS Division of Fluid Dynamics Meeting Abstracts, APS Meeting Abstracts, 2016, p. H10.007.
- [37] K. Gkaragkounis, E. Papoutsis-Kiachagias, K. Giannakoglou, Adjoint-assisted Pareto front tracing in aerodynamic and conjugate heat transfer shape optimization, *Comput. Fluids* 214 (2021) 104753.
- [38] V. Subramaniam, T. Dbouk, J.-L. Harion, Topology optimization of conjugate heat transfer systems: a competition between heat transfer enhancement and pressure drop reduction, *Int. J. Heat Fluid Flow* 75 (2019) 165–184.
- [39] F. Menter, Zonal two equation  $k - \omega$  turbulence models for aerodynamic flows, in: 23rd AIAA Fluid Dynamics, Plasmadynamics, and Lasers Conference, Orlando, FL, US, 1993, p. 2906.
- [40] Y. Notay, An aggregation-based algebraic multigrid method, *Electron. Trans. Numer. Anal.* 37 (2010) 123–146.
- [41] F. Giannetti, P. Luchini, Structural sensitivity of the first instability of the cylinder wake, *J. Fluid Mech.* 581 (1) (2007) 167–197.
- [42] P. Luchini, A. Bottaro, Adjoint equations in stability analysis, *Annu. Rev. Fluid Mech.* 46 (2014) 493–517.
- [43] H. Jonsson, B. Moshfegh, Modeling of the thermal and hydraulic performance of plate fin, strip fin, and pin fin heat sinks influence of flow bypass, *IEEE Trans. Compon. Packag. Technol.* 24 (2) (2001) 142–149.
- [44] D. Agonafer, D. Moffat, Numerical modeling of forced convection heat transfer for modules mounted on circuit boards, *ASME J. Electron. Packag.* 112 (1990) 333–337.
- [45] Y. Fu, P. Hall, N. Blackaby, On the Görtler instability in hypersonic flows: sutherland law fluids and real gas effects, *Philos. Trans. R. Soc. Lond. Ser. A* 342 (1993) 325–377.